Supplementary information

BiLayerStacker: A Universal and Global Program for Determining Ground-State Stacking Configurations of Bilayer 2D Nanomaterials

Yanchang Zhang[#]*, Liying Cui* [#]*, Jizhuo Duan, Bowen Sun, Danning Sun, Miao Du, Qian Wang* & *Bing Zheng**

Y. C. Zhang, L. Y. Cui, J. Z. Duan, B. W. Sun, D. N. Sun, M. Du, Q. Wang, Prof. B. Zheng
Key Laboratory of Functional Inorganic Materials Chemistry (Ministry of Education), School of Chemistry and Materials Science, Heilongjiang University, Harbin, 150080, P. R. China.
E-mail: zhengbing0106@163.com, zhengbing@hlju.edu.cn (B. Z.)

Contents of the Supplementary Information

Supplementary Notes

Supplementary Figures

Supplementary Tables

Supplementary Note 1

Bayesian optimization for the optimal interlayer distance

To determine the optimal interlayer distance (d_i) for each bilayer sliding-stacking configuration (“TD”, “TD′”, “T′D”, and “T′D′”; with lateral shift parameters $w_i = 0°$ and $s_j = 0$ Å), BiLayerStacker incorporates a Bayesian optimization algorithm. The obtained d_i values are then adopted as the initial interlayer distance for the corresponding stacking configurations. The Bayesian optimization process comprises four key steps: (1) total energy calculation and initial dataset construction, (2) dataset partitioning and Gaussian Process Regression (GPR) model training, (3) sampling point selection and single-point energy calculation, and (4) model iteration and optimal distance identification.

(1) Total energy calculation and initial dataset construction

For each stacking configuration (“TD”, “TD′”, “T′D”, and “T′D′”; $w_i = 0°$, $s_j = 0$ Å), BiLayerStacker randomly selects 12 interlayer distances (d) within the range of 1–12 Å and automatically generates the corresponding bilayer structures. Based on these structures, the software employs the ASE to invoke VASP and perform single-point energy calculation for total energy (E_{total}). The resulting (d, E_{total}) pairs form the initial dataset (as shown in step (1) of Supplementary Fig. 2), providing the basis for GPR model training.

(2) Dataset partitioning and GPR model training

The initial dataset is split into training and test sets at a ratio of 8 : 2. The GPR model is then trained on the training set to learn the relationship between d and E_{total} (see step (2) in Supplementary Fig. 2). Besides predicting the energy, the GPR model provides confidence intervals—quantified by the standard deviation $\sigma(d)$—to evaluate the uncertainty of its predictions. Larger confidence intervals indicate higher uncertainty, while narrower intervals suggest more reliable predictions. In Supplementary Fig. 2a, “Prediction” denotes the predicted mean energy $\mu(d)$, “Observations” represent the known data points (d, E_{total}), and the “Objective function” is the interpolated energy profile derived from existing samples. To enhance the model’s robustness, Bayesian optimization prioritizes sampling in regions of high uncertainty.

(3) Sampling point selection and single-point energy calculation

After the initial GPR fitting, BiLayerStacker adopts the Expected Improvement (EI) acquisition function (step (3) in Supplementary Fig. 2) to identify the interlayer distance d_{next} that is most likely to yield an improved prediction. The EI value is computed based on the GPR model's predicted mean $\mu(d)$ and standard deviation $\sigma(d)$. In each optimization iteration, the peak of the EI curve determines d_{next}, which is subjected to a new round of first-principles calculations to obtain the corresponding E_{total}. The new data point (d_{next}, E_{total}) is then appended to the training set to retrain the GPR model (step (3) in Supplementary Fig. 2), iteratively improving its predictive accuracy.

(4) Model iteration and optimal distance identification

As the GPR model is iteratively updated and the dataset expands, its ability to accurately predict the E_{total} improves. Once the confidence intervals across all candidate d values converge below a preset threshold ($\sigma < 5 \times 10^{-3}$ eV), the Bayesian optimization process is considered complete. The interlayer distance corresponding to the lowest predicted E_{total} is selected as the optimal d_i for that stacking configuration (step (4) in Supplementary Fig. 2).

Supplementary Note 2

Rationale for systematic study on bilayer borophene sliding-stacking configurations

As an emerging 2D nanomaterial, borophene has attracted considerable attention due to its rich structural diversity and unique physicochemical properties[1-7]. With exceptionally high thermal conductivity[1-3], outstanding mechanical strength[4], distorted Dirac fermions[5], and phonon-mediated superconductivity[6, 7], it is a promising candidate for stacking engineering studies. In previous studies, various monolayer borophene phases—such as α-[8, 9], β_{12}-[10-12], β-[13], β_1-[14], β_8-[13], β_{13}-[15], δ_3-[16, 17], δ_6-[16], χ_6-[18, 19], and χ_3-borophene[10, 11, 20]—have been successfully synthesized on metal substrates including Cu(111), Ag(111)/(110)/(100), Al(111), Au(111), and Ir(111), using techniques such as molecular beam epitaxy (MBE)[10], atomic layer deposition (ALD)[17], and chemical vapor deposition (CVD)[21]. Although these monolayer structures show favorable stability on substrates, their stability deteriorates rapidly when exposed to air or when the substrate is removed, which severely limits their practical applications in devices. It was not until 2021 that the realization of bilayer α-borophene[22] and β_{12}-like borophene[23] was achieved on Ag(111) and Cu(111) substrates via the MBE method. Despite exhibiting slightly improved thermodynamic stability compared to their monolayer counterparts, these bilayer structures still suffer from poor stability when exposed to ambient conditions or removed from the substrate, posing similar challenges for device integration. To overcome this constraint, the development of freestanding and highly stable multilayer borophene is critically important.

Through direct exfoliation techniques, monolayer β_{12}- and χ_3-borophene structures have been successfully fabricated[24, 25]. However, free-standing atomically well-defined bilayer borophenes remain unreported, let alone experimental investigations into their sliding-stacking engineering. Recent theoretical studies demonstrate that increasing layer number further enhances the stability of α-, α_5-, α_7-, and α_8-borophene[24, 25], underscoring layer number's critical role in their stability. Nevertheless, rigorous theoretical studies on bilayer borophene sliding-stacking engineering can not only identify ground-states in bilayer structures formed by different monolayer combinations but also clarify how stacking patterns correlate with stability—laying a foundation for understanding their intrinsic physicochemical properties. Given the large number of monolayer borophene structures, the number of bilayer stacking configurations formed by different monolayer combinations is correspondingly enormous, making the systematic study of bilayer sliding-stacking configurations extremely challenging. The exploration of conventional manual modeling methods for sliding-stacking combinations hardly captures the true ground-state sliding-stacking configurations[24, 25].

Therefore, the exploration of novel, intrinsically stable multilayer (especially bilayer) borophene configurations not only holds promise for facilitating experimental fabrication but also provides theoretical insights for structure modulation in stacking engineering. To the best of our knowledge, no prior studies have reported a comprehensive global search or ground-state identification of bilayer borophene sliding-stacking configurations. A systematic theoretical investigation into the stacking modes and stability landscape of bilayer borophene is of great significance, potentially unlocking new avenues for its device-level applications.

Supplementary Note 3

The definition of binding energy

The binding energy E_b is used to assess the thermodynamic stability of bilayer 2D nanomaterials and is defined as Equation (S1).

$$E_{\mathrm{b}} = -\frac{1}{i} E_{\mathrm{total}} + E_{\mathrm{atom}} \qquad \text{(S1)}$$

where E_{total} is the total energy of the bilayer 2D nanomaterials, i is the number of atoms, and E_{atom} is the energy of an isolated atom.

Supplementary Note 4

The definition of average in-plane binding energy

The average in-plane binding energy E_p of a bilayer 2D system is defined as Equation (S2).

$$E_\mathrm{p} = \frac{1}{n}\left(\sum_{n=1}^{n} \frac{E_{\mathrm{b}n}}{i}\right) \tag{S2}$$

where $E_{\mathrm{b}n}$ and i represent the binding energy and number of atoms of the isolated monolayer in the n^{th} layer of the 2D nanomaterial, respectively.

Supplementary Note 5

The definition of interlayer interaction energy

The interlayer interaction energy E_m quantifies the energetic contribution associated with forming a bilayer 2D material from two individual monolayers. It reflects the strength of interlayer coupling between the upper and lower layers, and is defined as Equation (S3).

$$E_m = (E_D + E_T) - E_{total} \tag{S3}$$

where E_{total} denotes the single-point total energy of the bilayer 2D nanomaterial, E_D and E_T refers to the single-point total energies of the lower and upper layers, respectively.

Supplementary Note 6

A discussion of four types of multi-center interlayer B–B bonds in borophene

Previous studies have identified four distinct types of multi-center interlayer B–B bonds in borophene systems, each with different structural motifs and bonding strengths[26, 27]. Type I involves loosely cross-linked mono-6-center bonds connected via small rings. Type II features loosely cross-linked bi-6-center bonds. Type III corresponds to tightly connected 6-center bonds, while Type IV involves tightly bound 4-center bonds. The relative bonding strength follows the order: Type IV < Type I < Type II < Type III. These interlayer bonding motifs play a critical role in modulating the structural and energetic landscape of bilayer borophene.

Supplementary Note 7

The definition of work function

Work function is a fundamental and important physical quantity in surface science, defined in solid state physics as the minimum amount of energy required to move an electron from the interior of a solid to the surface. In theoretical calculations, this physical quantity is expressed using Equation (S4).

$$\phi = E_{\mathrm{vac}} - E_{\mathrm{F}} \tag{S4}$$

where ϕ represents the work function of the system, where E_{vac} and E_{F} denote the vacuum and Fermi level of the system, respectively[28]. The work function depends not only on the electronic properties of the crystal but also on the features of the surface, such as Miller indices[28], surface functional group modifications[29], and surface dipole moments[30-35]. In the absence of adsorbed atoms or molecules on the surface, the intrinsic internal polarity of the compound can also give rise to a dipole at the surface, thereby affecting the work function[30-35]. Materials with both high and low work functions have important applications. Materials with low work functions can be applied to displays, electron guns, and catalysts, whereas materials with high work function can be used in electrodes, photovoltaic devices, and so on[36, 37].

Supplementary Figures

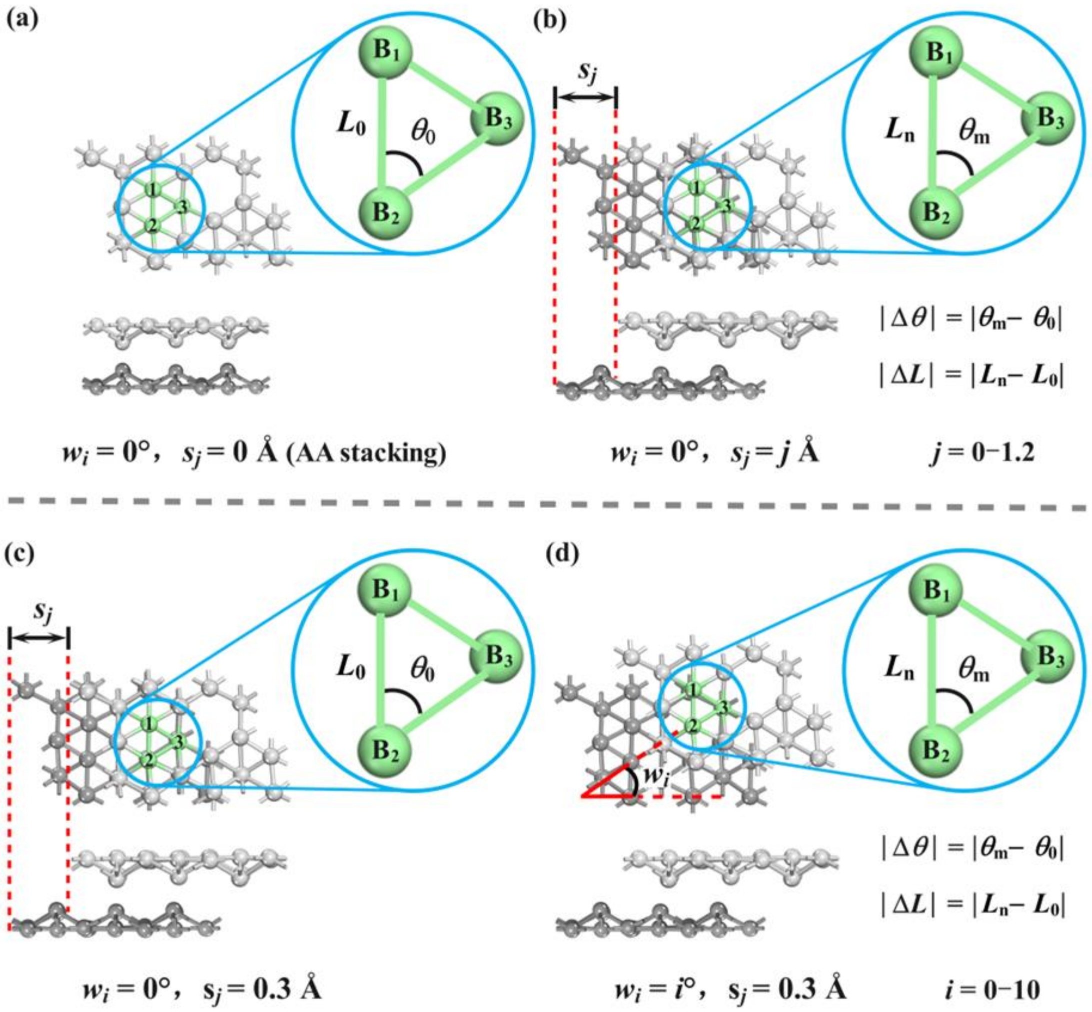

Supplementary Figure 1 Pre-screening of sliding distance step size and sliding angle step size using bilayer α_7-borophene as an example: top and side views of (a) the AA stacking configuration, (b) sliding configuration with a sliding angle of 0° and sliding distance of j Å, (c) the sliding configuration with a sliding angle of 0° and a sliding distance of 0.3 Å, (d) the sliding configuration with a sliding angle of i° and a sliding distance of 0.3 Å, L_0 and θ_0 denote the B_1–B_2 bond length and the bond angle $\angle B_1B_2B_3$ in the top layer of the initial stacking configuration, respectively; L_n and θ_m represent the corresponding bond length and bond angle in the upper layer of the sliding configuration, respectively; w_i and s_j denote the step sizes of sliding angle and sliding distance, respectively. $|\Delta L|$ and $|\Delta\theta|$ indicate the absolute differences in bond length and bond angle between the initial and sliding configurations.

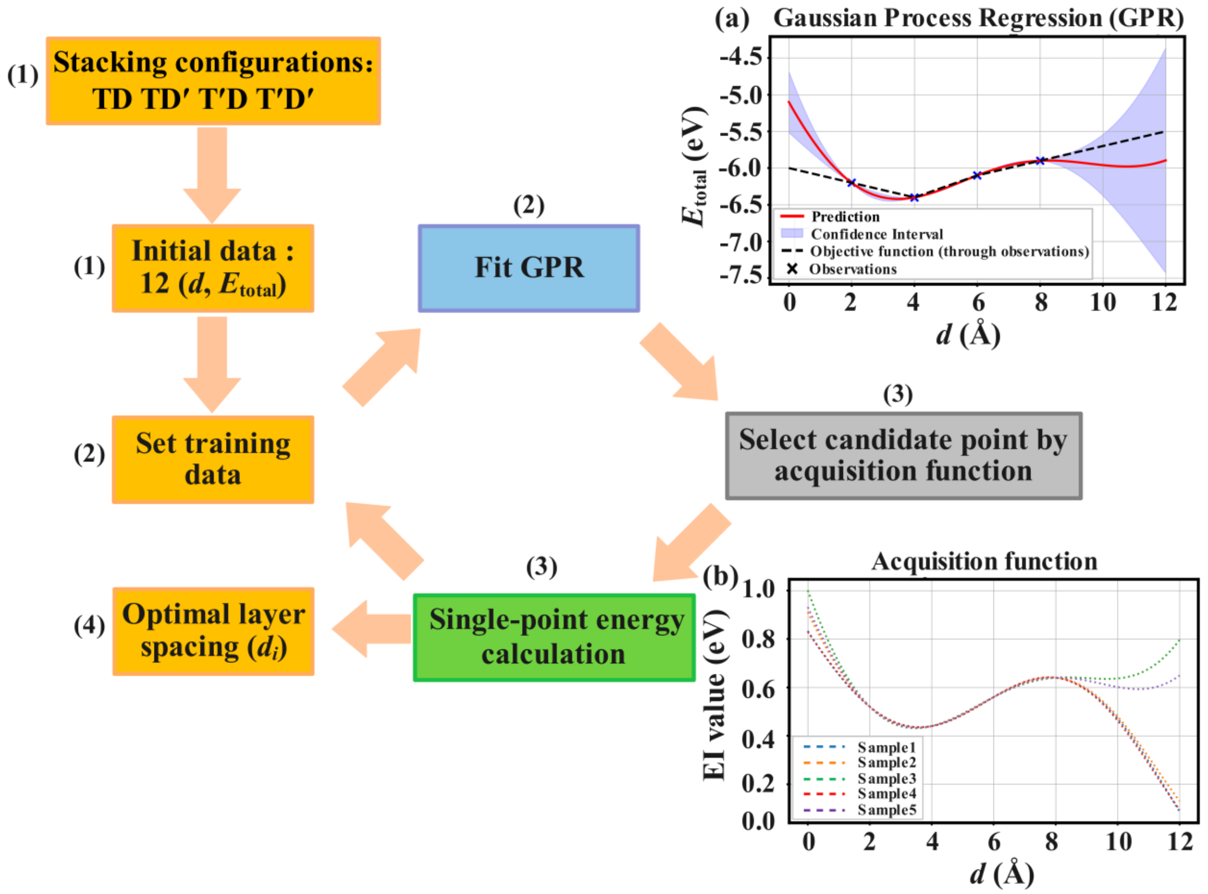

Supplementary Figure 2 Bayesian optimization workflow for predicting the optimal interlayer distance (d_i) of bilayer stacking configurations: (1) total energy calculation and initial dataset construction, (2) dataset partitioning and Gaussian process regression (GPR) model training, (3) sampling point selection and single-point energy calculation, and (4) iterative model refinement and optimal distance determination; (a) GPR-based fitting of the interlayer distance–total energy relationship, and (b) evolution of the expected improvement (EI) acquisition function with interlayer distance over different optimization iterations.

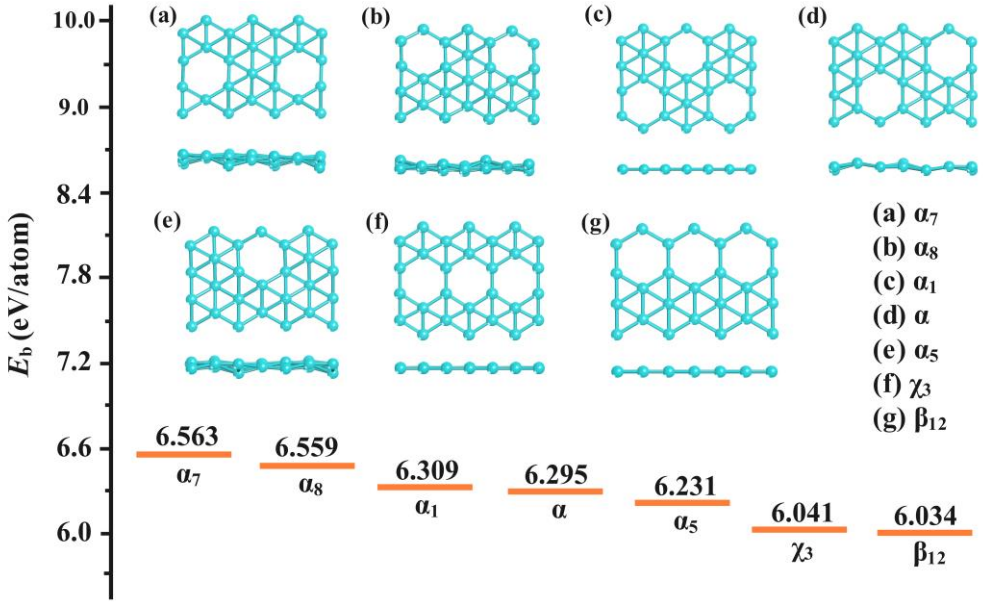

Supplementary Figure 3 Top and side views, along with the binding energies (E_b) of monolayer (a) α_7-, (b) α_8-, (c) α_1-, (d) α-, (e) α_5-, (f) χ_3-, and (g) β_{12}-borophene.

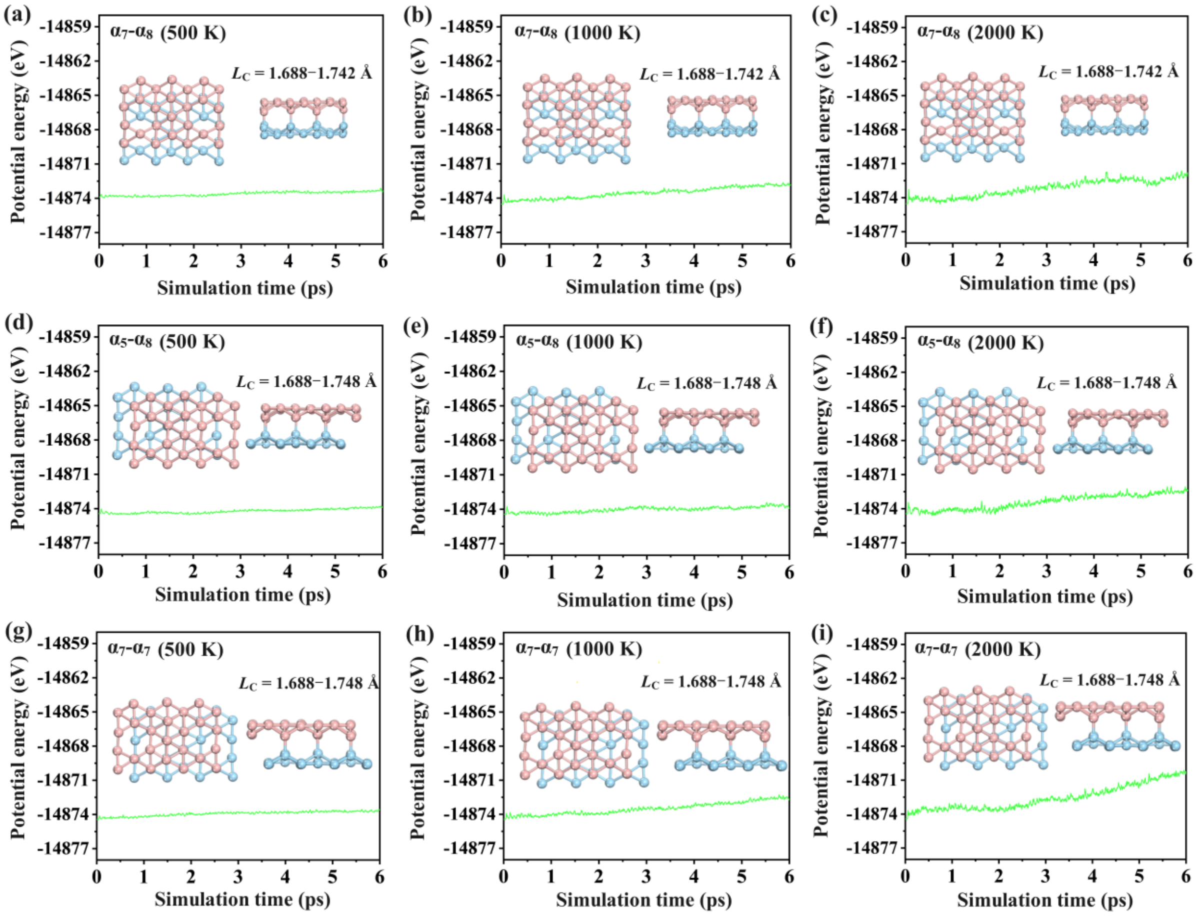

Supplementary Figure 4 Potential energies of bilayer (a)–(c) α_7-α_8-, (d)–(f) α_5-α_8-, and (g)–(i) α_7-α_7-borophene during 6 ps AIMD simulations at different temperatures (500 K, 1000 K, and 2000 K). Thermostat: Nosé-Hoover chain; time step: 1.5 fs; Nosé Q ratio = 2.0. L_c denotes the bond length range of interlayer bonded boron atoms.

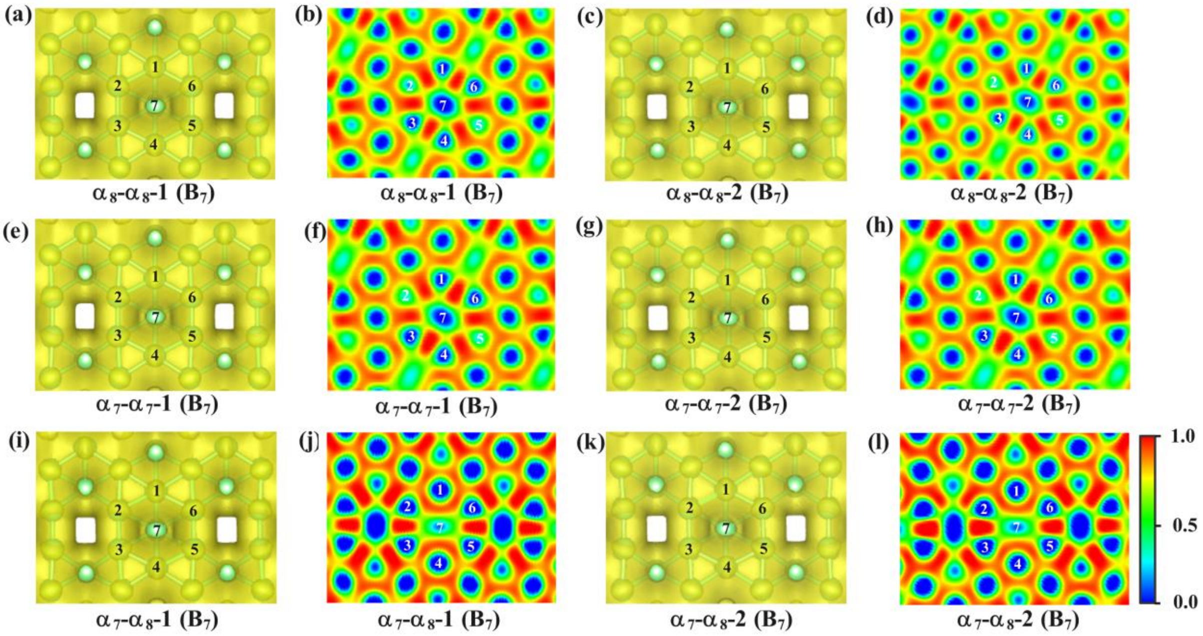

Supplementary Figure 5 Electron localization function (ELF) of B_7 for three representative bilayer borophene structures (α_8-α_8, α_7-α_7, and α_7-α_8); 3D ELF top views of top and down layers of (a), (c) α_8-α_8 (α_8-α_8-1 and α_8-α_8-2, respectively), (e), (g) α_7-α_7 (α_7-α_7-1 and α_7-α_7-2, respectively), and (i), (k) α_7-α_8 (α_7-α_8-1 and α_7-α_8-2, respectively); in-plane ELF slice views (Slice $B_1B_3B_5$) of (b) α_8-α_8-1, (d) α_8-α_8-2, (f) α_7-α_7-1, (h) α_7-α_7-2, (j) α_7-α_8-1, and (l) α_7-α_8-2; the isosurface value used is 0.20.

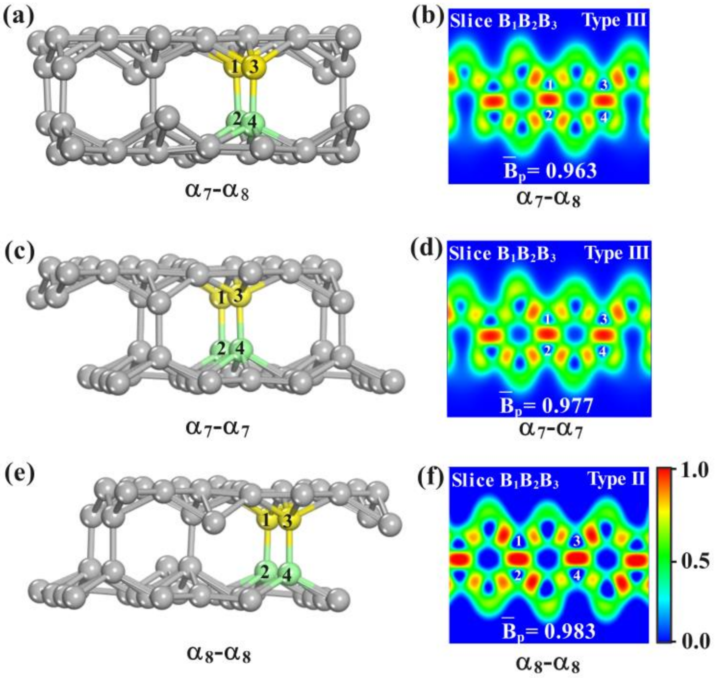

Supplementary Figure 6 The ELF of three representative bilayer borophene structures (α_7-α_8, α_7-α_7, and α_8-α_8). Side views of bilayer borophene structures of (a) α_7-α_8, (c) α_7-α_7, and (e) α_8-α_8; ELF slice views of interlayer B–B bonds for (b) α_7-α_8, (d) α_7-α_7, and (f) α_8-α_8, respectively; green and yellow spheres represent the boron atoms involved in interlayer bonding, and the $\bar{B}_p$ represents the average interlayer B–B bond population.

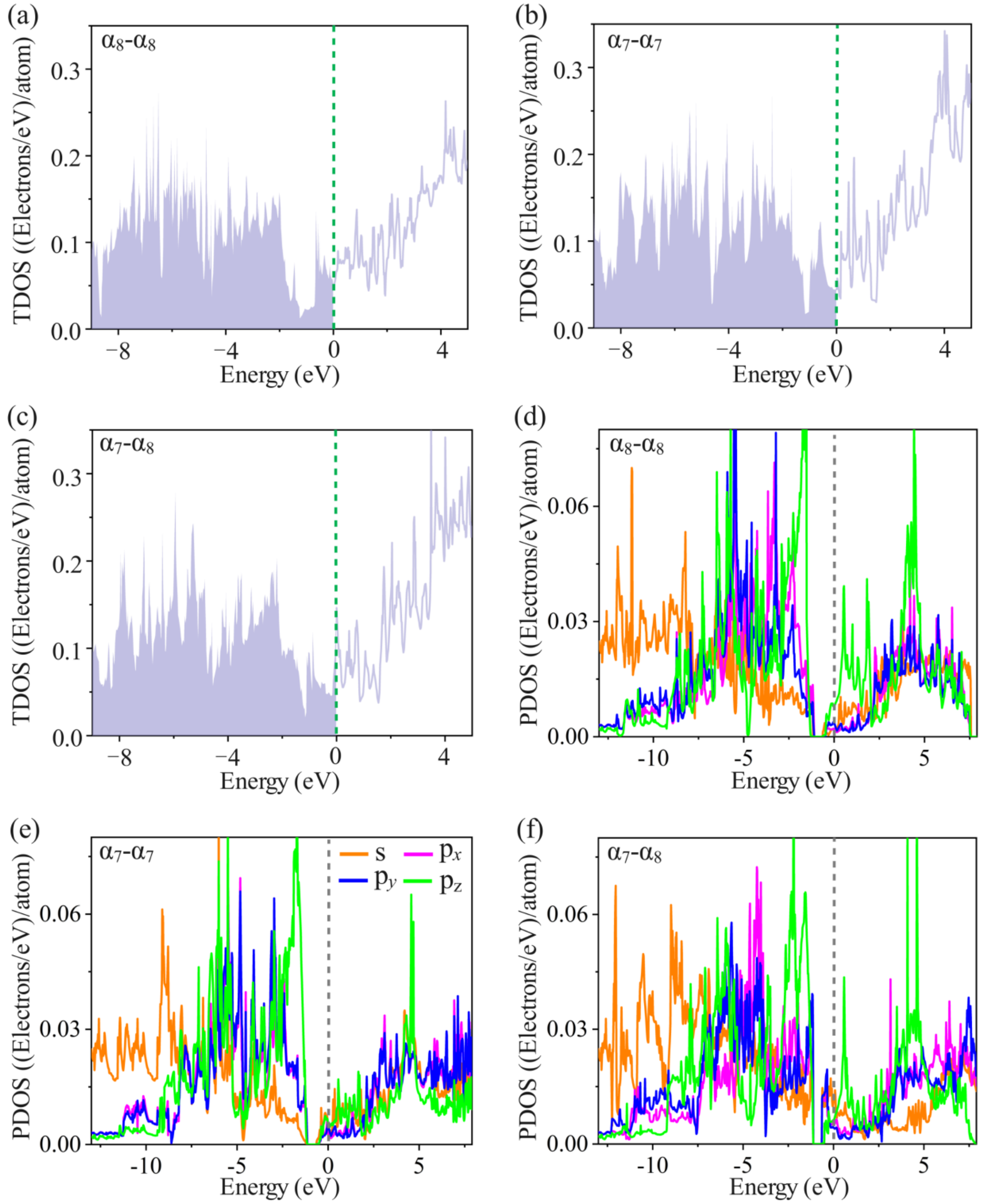

Supplementary Figure 7 Normalized total density of states (TDOS) for bilayer (a) α_8-α_8-, (b) α_7-α_7-, and (c) α_7-α_8-borophene and normalized interlayer partial density of states (PDOS) for bilayer (d) α_8-α_8-, (e) α_7-α_7-, and (f) α_7-α_8-borophene.

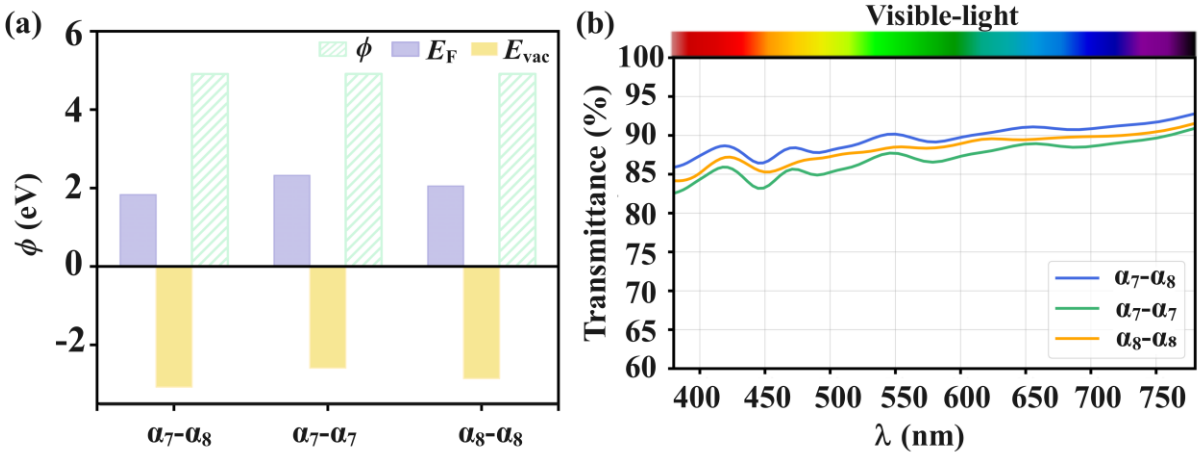

Supplementary Figure 8 (a) Work functions (ϕ), Fermi energy levels (E_F), and vacuum energy levels (E_{vac}) and (b) the visible light transmittance of bilayer α_8-α_8-, α_7-α_7-, and α_7-α_8-borophene.

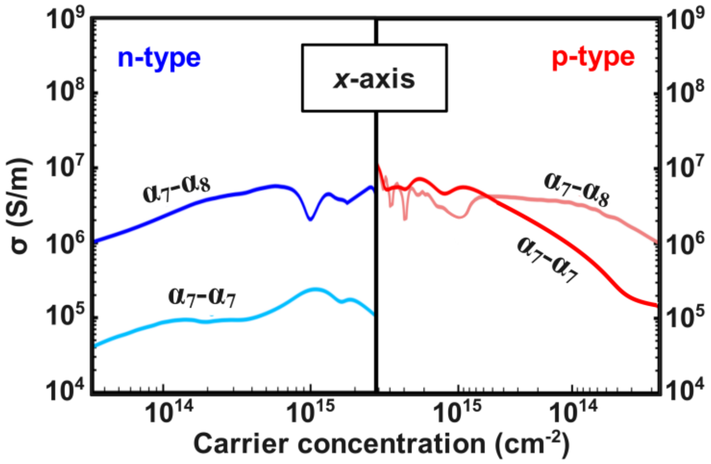

Supplementary Figure 9 The electrical conductivities (σ) of different carrier concentrations for bilayer α_7-α_7- and α_7-α_8-borophene.

Supplementary Tables

Supplementary Table 1. In-plane B–B bond populations of two hexagonal holes (B_6) in each layer of three representative bilayer borophene structures (α_7-α_8, α_8-α_8, and α_7-α_7). $\bar{B}_{pn}$ and $\bar{B}_p$ represent the average B–B bond population within a single B_6 unit and the average over all four B_6 units in the bilayer, respectively. α_n-α_m-1 and α_n-α_m-2 denote the top and down layers of the bilayer borophene (n, m = 7, 8), while B_6-1 and B_6-2 refer to the two B_6 motifs within each layer.

Structure	Motif	B_1–B_2	B_2–B_3	B_3–B_4	B_4–B_5	B_5–B_6	B_6–B_1	$\bar{B}_{pn}$	$\bar{B}_p$
α_7-α_8-1	B_6-1	1.09	0.98	1.02	1.09	1.08	0.98	1.040	0.987
	B_6-2	1.09	0.83	1.02	0.86	1.08	0.83	0.952	
α_7-α_8-2	B_6-1	0.92	0.93	1.14	1.14	0.93	1.07	1.022	
	B_6-2	0.89	0.84	1.02	0.89	1.08	0.89	0.935	
α_7-α_7-1	B_6-1	0.62	1.25	0.62	0.61	1.25	0.61	0.830	0.820
	B_6-2	0.62	1.25	0.62	0.61	1.25	0.61	0.830	
α_7-α_7-2	B_6-1	0.61	1.25	0.61	0.62	1.15	0.62	0.810	
	B_6-2	0.61	1.25	0.61	0.62	1.15	0.62	0.810	
α_8-α_8-1	B_6-1	0.61	1.12	0.60	0.61	1.12	0.60	0.777	0.804
	B_6-2	0.83	0.98	0.62	0.83	0.98	0.62	0.810	
α_8-α_8-2	B_6-1	0.60	1.15	0.62	0.60	1.15	0.62	0.790	
	B_6-2	0.74	1.15	0.62	0.74	1.15	0.62	0.837	

Supplementary Table 2. In-plane B–B bond populations of B_6 skeletons of the B_7 motifs in each layer of three representative bilayer borophene structures (α_7-α_8, α_8-α_8, and α_7-α_7) and the average of all in-plane B–B bonds in the bilayer system. $\bar{B}_{pn}$, $\bar{B}_{p}$, and $\bar{B}_{ps}$ represent the average B–B bond population of the B_6 skeletons within a single B_7 motif, the average of $\bar{B}_{pn}$ over all four B_7 motif in the bilayer, and the average of all in-plane B–B bonds in the bilayer system, respectively; α_n-α_m-1 and α_n-α_m-2 denote the top and down layers of the bilayer borophene (n, m = 7, 8), while B_7-1 and B_7-2 refer to the two B_7 motifs within each layer.

Structure	Motif	B_1–B_2	B_2–B_3	B_3–B_4	B_4–B_5	B_5–B_6	B_6–B_1	$\bar{B}_{pn}$	$\bar{B}_{p}$	$\bar{B}_{ps}$
α_7-α_8-1	B_7-1	0.87	1.25	0.90	0.83	1.25	0.87	0.963	0.955	0.856
	B_7-2	0.86	1.24	0.89	0.84	1.25	0.88	0.993		
α_7-α_8-2	B_7-1	0.89	1.24	0.85	0.84	1.24	0.89	0.955		
	B_7-2	0.84	0.98	0.83	0.84	1.09	0.88	0.910		
α_7-α_7-1	B_7-1	0.82	0.81	0.85	0.81	0.82	0.84	0.825	0.829	0.821
	B_7-2	0.81	0.82	0.84	0.82	0.83	0.84	0.826		
α_7-α_7-2	B_7-1	0.81	0.82	0.94	0.82	0.78	0.85	0.837		
	B_7-2	0.82	0.81	0.93	0.82	0.86	0.85	0.827		
α_8-α_8-1	B_7-1	0.81	0.85	0.82	0.85	0.82	0.81	0.827	0.827	0.810
	B_7-2	0.81	0.84	0.82	0.83	0.82	0.81	0.822		
α_8-α_8-2	B_7-1	0.83	0.84	0.82	0.85	0.82	0.83	0.831		
	B_7-2	0.82	0.84	0.82	0.84	0.82	0.83	0.828		

Supplementary Table 3. Interlayer B–B bond populations of bilayer α_7-α_8-, α_7-α_7-, and α_8-α_8-borophene structures. *n*, *m*, and $\bar{\mathrm{B}}_\mathrm{p}$ denote the number of interlayer B–B bonds, the number of interlayer bonded boron atoms, and the average interlayer B–B bond populations, respectively.

Structure	*n*	*m*	Layer	Bond population			$\bar{\mathrm{B}}_\mathrm{p}$
α_7-α_8	3	6	1−2	0.96	0.97	0.96	0.963
α_7-α_7	3	6	1−2	0.97	0.97	0.99	0.977
α_8-α_8	3	6	1–2	0.99	0.97	0.99	0.983

References

1. Li D. F., *et al.* 2D Boron sheets: structure, growth, and electronic and thermal transport properties. *Adv. Funct. Mater.* **30**, 32 (2020).
2. Li D., *et al.* Stretch-driven increase in ultrahigh thermal conductance of hydrogenated borophene and dimensionality crossover in phonon transmission. *Adv. Funct. Mater.* **28**, 1801685 (2018).
3. Xie Z., *et al.* Chemistry, functionalization, and applications of recent monoelemental two-dimensional materials and their heterostructures. *Chem. Rev.* **122**, 1127-1207 (2022).
4. Zarechnaya E. Y., *et al.* Superhard semiconducting optically transparent high pressure phase of boron. *Phys. Rev. Lett.* **102**, 185501 (2009).
5. Xu J., *et al.* Ultrathin single-crystalline boron nanosheets for enhanced electro-optical performances. *Adv. Sci.* **2**, 1500023 (2015).
6. Wang Z.-Q., *et al.* Review of borophene and its potential applications. *Front. Phys.* **14**, 33403 (2019).
7. Kaneti Y. V., *et al.* Borophene: two-dimensional boron monolayer: synthesis, properties, and potential applications. *Chem. Rev.* **122**, 1000-1051 (2022).
8. Kiraly B., *et al.* Borophene synthesis on Au(111). *ACS Nano* **13**, 3816-3822 (2019).
9. Tang H., Ismail-Beigi S. Novel precursors for boron nanotubes: the competition of two-center and three-center bonding in boron sheets. *Phys. Rev. Lett.* **99**, 115501 (2007).
10. Feng B., *et al.* Experimental realization of two-dimensional boron sheets. *Nat. Chem.* **8**, 564-569 (2016).
11. Liu X., *et al.* Intermixing and periodic self-assembly of borophene line defects. *Nat. Mater.* **17**, 783 (2018).
12. Li Q., *et al.* Synthesis of quantum-confined borophene nanoribbons. *ACS Nano* **18**, 483-491 (2023).
13. Zhong Q., *et al.* Synthesis of borophene nanoribbons on Ag(110) surface. *Phys. Rev. Mater.* **1**, 021001 (2017).
14. Wu X. J., *et al.* Two-dimensional boron monolayer sheets. *ACS Nano* **6**, 7443-7453 (2012).
15. Wu R., Gozar A., Bozovic I. Large-area borophene sheets on sacrificial Cu(111) films promoted by recrystallization from subsurface boron. *npj Quantum Mater.* **4**, 40 (2019).
16. Li W., *et al.* Experimental realization of honeycomb borophene. *Sci. Bull.* **63**, 282-286 (2018).

17. Mannix A. J., *et al.* Synthesis of borophenes: anisotropic, two-dimensional boron polymorphs. *Science* **350**, 1513-1516 (2015).
18. Vinogradov N. A., *et al.* Single-phase borophene on Ir(111): formation, structure, and decoupling from the support. *ACS Nano* **13**, 14511-14518 (2019).
19. Omambac K. M., *et al.* Segregation-enhanced epitaxy of borophene on Ir(111) by thermal decomposition of borazine. *ACS Nano* **15**, 7421-7429 (2021).
20. Wu R., *et al.* Large-area single-crystal sheets of borophene on Cu(111) surfaces. *Nat. Nanotechnol.* **14**, 44 (2019).
21. Zhong Q., *et al.* Metastable phases of 2D boron sheets on Ag(111). *J. Phys.:Condens. Matter* **29**, 095002 (2017).
22. Liu X., *et al.* Borophene synthesis beyond the single-atomic-layer limit. *Nat. Mater.* **21**, 35 (2022).
23. Chen C., *et al.* Synthesis of bilayer borophene. *Nat. Chem.* **14**, 25 (2022).
24. Wang Z., *et al.* Prediction of two freestanding metallic 3−5-layer borophene. *Surf. Interfaces* **56**, 13 (2025).
25. Zheng B., *et al.* Ultra-stable metallic freestanding multilayer borophene with tunable work function. *Appl. Surf. Sci.* **612**, 15 (2023).
26. Galeev T. R., *et al.* Deciphering the mystery of hexagon holes in an all-boron graphene α-Sheet. *Phys. Chem. Chem. Phys.* **13**, 11575-11578 (2011).
27. He J., *et al.* Effects of adatom species on the structure, stability, and work function of adatom-α-borophene nanocomposites. *Phys. Chem. Chem. Phys.* **24**, 8923-8939 (2022).
28. Greiner M. T., *et al.* Transition metal oxide work functions: the influence of cation oxidation State and oxygen vacancies. *Adv. Funct. Mater.* **22**, 4557-4568 (2012).
29. Khazaei M., *et al.* OH-Terminated Two-dimensional transition metal carbides and nitrides as ultralow work function materials. *Phys. Rev. B* **92**, 10 (2015).
30. Kolb D., M., Przasnyski M., Gerischer H. Underpotential deposition of metals and work function differences. *J. Electroanal. Chem. Interfacial Electrochem.* **54**, 25-38 (1974).
31. Zhu J., *et al.* Properties of two-dimensional insulators: a DFT study of bimetallic oxide CrW_2O_9 clusters adsorption on MgO ultrathin films. *Appl. Surf. Sci.* **379**, 213-222 (2016).
32. Huang J. S., Xu Z., Yang Y. Low-work-function surface formed by solution-processed and thermally deposited nanoscale layers of cesium carbonate. *Adv. Funct. Mater.* **17**, 1966-1973 (2007).
33. Prada S., Martinez U., Pacchioni G. Work function changes induced by deposition of ultrathin dielectric films on metals: a theoretical analysis. *Phys. Rev. B* **78**, 8 (2008).

34. Martinez U., *et al.* Tailoring the interaction strength between gold particles and silica thin films via work function control. *Phys. Rev. Lett.* **103**, 4 (2009).
35. Prada S., Giordano L., Pacchioni G. Li, Al, and Ni substitutional doping in MgO ultrathin films on metals: work function tuning via charge compensation. *J. Phys. Chem. C* **116**, 5781-5786 (2012).
36. Stoessel M., *et al.* Impact of the cathode metal work function on the performance of vacuum-deposited organic light emitting-devices. *Appl. Phys. A* **68**, 387-390 (1999).
37. Tsiplakides, D. Work function and catalytic activity measurements of an IrO_2 film deposited on YSZ subjected to in situ electrochemical promotion. *J. Electrochem. Soc.* **145**, 905 (1998).